Modulational instability and resonant wave modes act on the metastability of oscillator chains

Torsten Gross,[1,*] Dirk Hennig,[2,†] and Lutz Schimansky-Geier[1,‡]
[1]*Department of Physics, Humboldt-Universität zu Berlin, D-12489 Berlin, Germany*
[2]*Department of Mathematics, University of Portsmouth, Portsmouth PO1 3HF, United Kingdom*
(Received 4 June 2014; published 22 September 2014)

We describe the emergence and interactions of breather modes and resonant wave modes within a two-dimensional ringlike oscillator chain in a microcanonical situation. Our analytical results identify different dynamical regimes characterized by the potential dominance of either type of mode. The chain is initially placed in a metastable state, which it can leave by passing over the brim of the applied Mexican-hat-like potential. We elucidate the influence of the different wave modes on the mean-first passage time. A central finding is that also in this complex potential landscape a fast noise-free escape scenario solely relying on nonlinear cooperative effects is accomplishable even in a low-energy setting.

DOI: 10.1103/PhysRevE.90.032919 PACS number(s): 05.45.Xt, 05.65.+b

I. INTRODUCTION

The interest in the escape of coupled degrees of freedom or chains of interacting units out of metastable states has been intensified lately [1–8]. Escape is accomplished when the considered object overcomes a potential barrier separating the local minimum of the potential landscape from a neighboring domain of attraction. The associated transition state corresponds to a saddle point in the potential landscape. Surmounting the energetic bottleneck requires a minimal amount of energy greater than the activation energy, which can be provided in two different ways. One is the possibility of stochastic escape occurring in the presence of a heat bath that is sampled for the optimal fluctuations triggering an event of escape [9,10]. The second one is that in the noise-free situation the energy can be supplied in a single shot under microcanonical circumstances.

Previous work [7,8] addressed microcanonical escape scenarios of chains of interacting units in one- and two-dimensional potential landscapes with a single barrier and compared those to the corresponding noise-assisted escape process. In the deterministic setting, a nonlinear breather dynamics assists at a speedy passage through the metastable transition state. If additionally noise and linear dissipation act on the chain and the friction is large, the escape rate becomes smaller. The breathers are then unable to grow out of the phonon background. In contrast for small friction when relaxation times become large, the breathers are able to survive and contribute as added noise to the amplification of the escape [8].

In this paper we extend these studies to systems of higher complexity and explore whether the observed phenomena are solely inherent to highly idealized settings or whether they remain relevant in a more general context. To this end, we investigate a ring of interacting units evolving in a Mexican-hat-like two-dimensional potential landscape. The emergence of breathers and resonant wave modes in the chain's dynamics is elucidated. Analytical results are derived that allow us to determine parameter choices, which accomplish an efficient noise-free escape scenario solely relying on nonlinear cooperative effects.

Apart from our conceptual interest in this work, the results can be applied to the description of microbubble surface modes. Microbubble surfaces can be modeled by a closely related system in which breather modes were verified experimentally [11]. Our results demonstrate the potential relevance of resonant wave modes and the escape behavior within this specific context.

The paper is organized as follows: In the next section the model of the ring of interacting units evolving in the Mexican-hat-like potential is introduced. Then, the formation of breather solutions initiated by modulational instability is considered, followed by the analysis of the resonant longitudinal wave modes and the interaction between the two. After establishing this theoretical framework, the subsequent section elucidates the deterministic escape scenario. Transition states and the associated escape channels are discussed in detail, followed by an investigation of the escape time statistics. Finally, we summarize our results.

II. LOCALIZED AND RESONANT WAVE MODES IN AN OSCILLATOR RING CHAIN MODEL

Motivated by the experimental studies in Ref. [11] we study a Rouse-like Hamiltonian system consisting of a ring chain of N linearly coupled oscillators of mass m subjected to an external Mexican-hat-like anharmonic potential $V(\mathbf{q}_i) = -a\sqrt{\mathbf{q}_i^2} + b\cos(\sqrt{\mathbf{q}_i^2}/\lambda)$. The ring chain ($\mathbf{q}_{N+1} = \mathbf{q}_1$ and $\mathbf{p}_{N+1} = \mathbf{p}_1$) is initially situated close to the bottom of the potential well. We are particularly interested in events of escape of the entire ring chain over the outer brim of the Mexican-hat-like potential. Rescaling coordinates, $\widetilde{\mathbf{q}}_i = (b/a)\,\mathbf{q}_i$, momenta, $\widetilde{\mathbf{p}}_i = \sqrt{m\,b}\,\mathbf{p}_i$, and time, $\tilde{t} = (\sqrt{m\,b}/a)\,t$, to natural units yields two remaining effective parameters, the coupling strength $\widetilde{\kappa} = (b/a^2)\,\kappa$ and the potential width parameter $\widetilde{\lambda} = (a/b)\,\lambda$, and leads to the Hamiltonian (tildes have been omitted),

$$\mathcal{H} = \sum_{i=0}^{N-1}\left[\frac{\mathbf{p}_i^2}{2} + \frac{\kappa}{2}(\mathbf{q}_i - \mathbf{q}_{i+1})^2 + V(\mathbf{q}_i)\right],$$

$$V(\mathbf{q}_i) = -\sqrt{\mathbf{q}_i^2} + \cos\left(\frac{\sqrt{\mathbf{q}_i^2}}{\lambda}\right), \tag{1}$$

*tgross@physik.hu-berlin.de
†dirk.hennig@port.ac.uk
‡alsg@physik.hu-berlin.de

 ©2014 American Physical Society

with the corresponding equations of motion

$$\ddot{\mathbf{q}}_i = -\kappa\,(2\,\mathbf{q}_i - \mathbf{q}_{i+1} - \mathbf{q}_{i-1}) + \frac{\mathbf{q}_i}{\sqrt{\mathbf{q}_i^2}} + \sin\left(\frac{\sqrt{\mathbf{q}_i^2}}{\lambda}\right)\frac{\mathbf{q}_i}{\lambda\sqrt{\mathbf{q}_i^2}} \quad i \in 0\ldots N-1, \tag{2}$$

and the coordinates and momenta are subject to periodic boundary conditions, $\mathbf{q}_{N-1} = \mathbf{q}_0$ and $\mathbf{p}_{N-1} = \mathbf{p}_0$.

The energy is conserved,

$$\mathcal{H}(\{\mathbf{p}(t)\},\{\mathbf{q}(t)\}) = \text{const.} = E.$$

That is, we consider deterministic dynamics under *micro-canonical* conditions when the energy initially allocated to the system has to suffice for the task performance and no additional coupling to a thermal bath or any other external sources assists the escape. This has to be distinguished from the experimental setup considered in Ref. [11], where energy is injected into the system by means of external parametric driving.

Considering the rotational symmetry of the Mexican-hat-like potential, it is convenient to express the equations of motion also in terms of radial and angular coordinates, r_i and φ_i,

$$\ddot{r}_i = r_i\,\dot{\varphi}_i^2 - \kappa\,[2\,r_i - r_{i+1}\cos(\varphi_i - \varphi_{i+1}) - r_{i-1}\cos(\varphi_{i-1} - \varphi_i)] + 1 + \frac{1}{\lambda}\sin\left(\frac{r_i}{\lambda}\right) \tag{3}$$

$$\ddot{\varphi}_i\,r_i = -2\,\dot{r}_i\,\dot{\varphi}_i + \kappa[r_{i-1}\sin(\varphi_{i-1} - \varphi_i) - r_{i+1}\sin(\varphi_i - \varphi_{i+1})]. \tag{4}$$

A. Stability of the minimum-energy configuration

Fixed points are found for the configuration $r_i = r^0$, $\varphi_i = i\,\Delta\Theta$, with $\Delta\Theta = 2\pi/N$, where a conditional equation for r^0 arises from setting all time derivatives in Eq. (3) to zero

$$0 = -2\,\kappa\,r^0\left[1 - \cos\left(\frac{2\,\pi}{N}\right)\right] + 1 + \frac{1}{\lambda}\sin\left(\frac{r^0}{\lambda}\right). \tag{5}$$

Initially, the ring chain is placed in the vicinity of this so-called minimum-energy configuration. In order for the ring chain to evolve from a metastable state, that is from a basin of potential energy, the fixed point needs to be (Lyapunov) stable. Consequently, we will need to limit our parameter space to the region of stability. The results of a linear stability analysis, see Appendix A, are represented in Fig. 1. It shows instability arising for large values of the coupling constant when the ring chain's tendency to contract becomes so strong that any small perturbation will initiate a contraction that pulls the entire ring chain over the central potential hump into the first potential valley (and possibly beyond).

As an additional constraint on the parameters, let us require the existence of the barrier in the Mexican-hat-like potential (see Fig. 2), which confines the range of the potential width parameter to $0 < \lambda < 1$ and in conjunction with a restriction of the coupling constant to $0 < \Delta\Theta^2\kappa < 1.3$ a sufficiently large region of stability in parameter space results. The number of oscillators will be kept at $N = 100$.

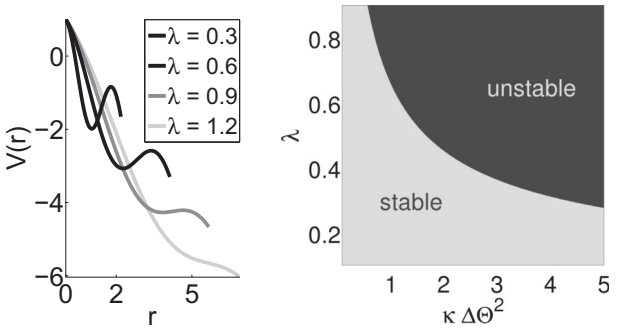

FIG. 1. The left-hand side of the figure represents the profile of the Mexican-hat-like potential. The potential barrier vanishes for $\lambda > 1$. The right-hand side of the figure shows the result of the stability analysis of the fixed point comprising the minimum-energy configuration and vanishing momenta for $N = 100$ (see Appendix A for details).

B. Modulational instability produces radial breathers

Initially, the oscillators are placed in a perturbed ringlike structure around the central potential hump (Fig. 2),

$$\mathbf{q}_i^{\mathrm{IC}} = r^{\mathrm{IC}}\cdot\begin{pmatrix}\cos(i\,\Delta\Theta)\\ \sin(i\,\Delta\Theta)\end{pmatrix} + \begin{pmatrix}\Delta q_i^x\\ \Delta q_i^y\end{pmatrix}, \quad \mathbf{p}_i^{\mathrm{IC}} = \begin{pmatrix}\Delta p_i^x\\ \Delta p_i^y\end{pmatrix},$$

where Δq_i^x and Δq_i^y as well as Δp_i^x and Δp_i^y are random perturbations taken from a uniform distribution within the intervals

$$\Delta q_i^x, \Delta q_i^y \in [-0.01,0.01]; \quad \Delta p_i^x, \Delta p_i^y \in [-0.01,0.01].$$

In this setting, the angular distance between any pair of neighboring oscillators is almost equal (close to $\Delta\Theta$) so that the initial angular acceleration is small. Thus, for short time periods after the system's preparation, virtually no variations of the angular variables, viz. $\varphi_i(t) = \varphi_i^0 = i\,\Delta\Theta$, are expectable. Moreover, for low-energy settings each oscillator's initial radius is close to r^0, so that the equation of motion for the radial components can be approximated by a Taylor expansion in r_i around $r_i = {r_i}^0$, where we neglect terms of order ${\Delta r_i}^3 = (r_i - r^0)^3$ and higher. Thus, as an approximation

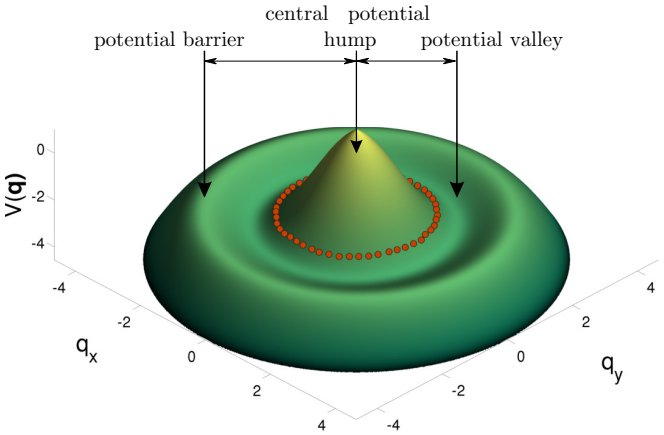

FIG. 2. (Color online) A typical initial preparation of the oscillator chain.

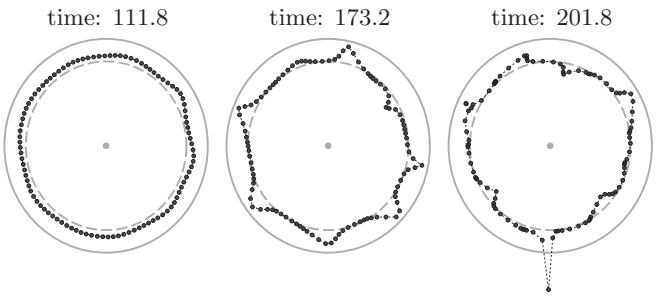

FIG. 3. Simulation snapshots showing the growth of a radial breather array from an almost homogeneous initial state due to modulational instability. The ongoing amplification of this pattern eventually drives an individual oscillator over the potential barrier and thus triggers an escape of type I as described in Sec. III. Parameters: $\kappa\,\Delta\Theta^2 = 0.79\times10^{-4}$, $\lambda = 0.85$.

for short periods of time after the initiation of the system, the angular components remain fixed and the evolution of the radial components is governed by the equation

$$\begin{aligned}\Delta\ddot{r}_i &= \kappa\left[\cos\left(\frac{2\pi}{N}\right)(\Delta r_{i+1}+\Delta r_{i-1}) - 2\,\Delta r_i\right]\\ &\quad -{\omega_0}^2\,\Delta r_i + \alpha\,{\Delta r_i}^2,\\ {\omega_0}^2 &= -\frac{1}{\lambda^2}\cos\left(\frac{r^0}{\lambda}\right),\quad \alpha = -\frac{1}{2\,\lambda^3}\sin\left(\frac{r^0}{\lambda}\right).\end{aligned}$$

In this case, the oscillators can only move along equally spaced rays that all emerge from the origin. Therefore, this approximation will be referred to as the starlike ring-chain model.

Due to the initial ringlike setup, the chain will first oscillate in a $k = 0$ phononlike manner. Typically, in our simulations we observe the emergence of a regularly spaced array of breathers, as shown in Fig. 3. These localized excitations play a crucial role because they concentrate energy in single degrees of freedom and, therefore, substantially influence the escape behavior, as will be discussed in Sec. III.

The studies in [12,13] reveal that the starlike chain model is able to describe the emergence of these transversal modes in terms of a modulational instability. The key idea herein is to formulate a discrete nonlinear Schrödinger equation (DNLS), also known as the discrete self-trapping equation [14], for a time-dependent amplitude of the first-harmonic phonon wave. Inspecting the stability of the DNLS's plane-wave solutions yields a dispersion relation for the small perturbation terms on the basis of which those wave modes on the oscillator chain that grow in amplitude and create the transversal pattern can be determined. We call the wave number and the angular frequency of the phonons k and ω, and those of the perturbations Q and Ω. Their dispersion relations read

$$\begin{aligned}&\omega^2 = \omega_0^2 + 2\kappa\,(1-\cos\Delta\Theta\,\cos k)\quad\text{and}\\ &(\omega_0\,\Omega - \kappa\cos\Delta\Theta\,\sin k\,\sin Q)^2\\ &\quad = \kappa\cos\Delta\Theta\,\cos k\sin^2\frac{Q}{2}\\ &\qquad\times\left(4\kappa\,\cos\Delta\Theta\,\cos k\,\sin^2\frac{Q}{2} - 2\gamma A^2\right).\end{aligned}\tag{6}$$

Equation (6) describes the stability of the Q-mode perturbation on the k-mode carrier wave. Q and k have a 2π periodicity and can therefore be chosen to be in the first Brillouin zone. Furthermore, we can restrict the range of k and Q: $k,Q \in [0,\pi]$, because negative values only correspond to waves with the opposite direction of propagation. The perturbations are stable for $\Omega \in \mathbb{R}$, which is the case when the right-hand side of Eq. (6) is positive. Since $\gamma \geqslant 0$, all carrier waves with $\cos k \leqslant 0 \Leftrightarrow k \in [\pi/2,\pi]$ are therefore stable with respect to any perturbation mode. For $k \in [0,\pi/2]$, perturbations will grow, provided that

$$\cos k\,\sin^2\left(\frac{Q}{2}\right) \leqslant \frac{A^2}{{A_0}^2}.\tag{7}$$

Here A is the phonon amplitude,

$${A_0}^2 = \frac{2\kappa\cos(\Delta\Theta)}{\gamma},\quad\text{and}\quad \gamma = \frac{10\alpha^2}{3{\omega_0}^2}.$$

We can then find an according growth rate

$$\begin{aligned}\widetilde{\Gamma}_r(Q) = |\mathrm{Im}(\Omega)| &= \frac{\sin\left(\frac{Q}{2}\right)}{\omega_0}\\ &\times\sqrt{2\kappa\,\gamma\cos k\left[A^2 - {A_0}^2\sin^2\left(\frac{Q}{2}\right)\cos k\right]}.\end{aligned}\tag{8}$$

The left-hand side of Eq. (7) is monotonically increasing as a function of Q. Thus, there is an upper bound, Q^*, such that for $Q > Q^*$ wave modes cannot be unstable. For $A^2 \leqslant 2\,{A_0}^2\cos k$ the function Eq. (8) attains its maximum at

$$Q_{\max} = 2\,\arcsin\sqrt{\frac{A^2}{2\,{A_0}^2\cos k}}.$$

If $Q_{\max} > Q^*$ then the most unstable mode arises for Q^* and for $A^2 > 2\,{A_0}^2\cos k$, the maximal growth rate is found at $Q = \pi$. The wave number associated with the maximal growth rate defines the spatial pattern of the forming breather array.

For our simulations the system is prepared in a flat initial state with small random perturbations, and hence $k = 0$. The phonon wave amplitude A is related to the energy of the system, E, through

$$E = \mathcal{H}\left(\{\mathbf{p}_i(t) = 0\},\{r_i = r^0 + A,\varphi_i = \varphi_i^0\}\right).\tag{9}$$

Combining Eqs. (5) and (9) allows us to calculate A for given energy E and system parameters. Eventually, the so found value of A determines the mode number and growth rate of the most unstable modulation. However, due to the periodic boundary conditions only a discrete spectrum of perturbative waves can occur,

$$Q = m_r\,\Delta\Theta\quad m_r \in 0,1\ldots(N-1),$$

where m_r denotes the possible mode numbers. To take account of this, we choose the wave number of the most unstable (continuous) mode as the nearest value lying in the corresponding unstable part of the discrete spectrum yielding the predicted mode number of the emerging transversal wave. Its dependence on the system parameters is represented in Fig. 5(a) together with the according growth rates in Fig. 5(b).

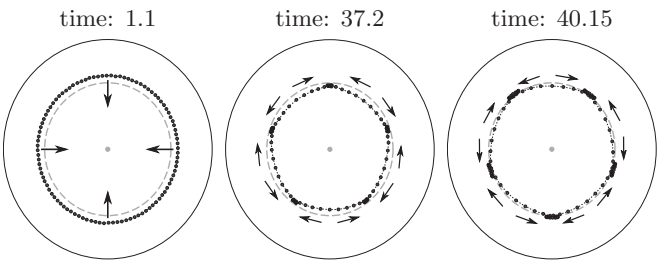

FIG. 4. Simulation snapshots showing the emergence of a longitudinal wave pattern with wave number $m_\varphi = 5$. Arrows indicate the chain movement. Parameters: $\kappa\,\Delta\Theta^2 = 0.06$, $\lambda = 0.4$.

C. Emergence of resonant longitudinal waves

The foregoing analysis characterizes the transversal wave pattern that arises from modulational instability on a $k = 0$ phonon background within the starlike chain model. This is an essential step in the understanding of the chain escape behavior, as discussed in Sec. III A. However, the basic assumption of fixed angular components seems only justified for short time periods. Obviously, the angular dynamics plays an increasingly important role as time proceeds. Remarkably, for most of the parameter choices the angular movement is far from being erratic but instead consists of regular and pronounced longitudinal wave patterns, as shown in Fig. 4. These patterns are fundamental for the characterization of the system's dynamics and its deterministic escape behavior.

Our analytic description of this phenomenon is motivated by the observation of periodic energy transfer between radial and longitudinal degrees of freedom when these modes appear; see the middle plot of Fig. 6. Typically, we first observe a few oscillations of the perturbed radial $k = 0$ phononlike mode until the longitudinal pattern grows in amplitude. This causes a decrease of the radial mode's amplitude. After a short time, the longitudinal amplitude decreases again. Thereby the energy is transferred back into the radial degrees of freedom and the entire process repeats.

Motivated by this observation we expect longitudinal waves to emerge in the presence of the $k = 0$ radial phononlike mode. This leads to the ansatz

$$r_i = r^0 + A\,\sin(\omega_0\, t) \equiv \tilde{r}^0(t), \tag{10}$$

with $A < r^0$. Note that this is not an exertion of (holonomic) constraints, which would lead to a new set of equations of motion. Instead, Eq. (10) serves as an approximation of the original system's radial dynamics.

It becomes more inaccurate as more energy is transferred into the angular degrees of freedom (as this reduces the amplitude of the $k = 0$ phonon) and the more the initial perturbations cause a deviation from a flat state. However, the aim is to describe a dynamical phenomenon that emerges from a setting where the error of the assumption is small.

Substituting the ansatz Eq. (10) into the angular equations of motion Eq. (4) yields

$$\ddot{\varphi}_i = -\gamma_\varphi(t)\,\dot{\varphi}_i + \kappa\,[\sin(\varphi_{i-1} - \varphi_i) - \sin(\varphi_i - \varphi_{i+1})]\,,$$

with $\gamma_\varphi(t) = 2\dot{\tilde{r}}^0(t)/\tilde{r}^0(t)$. We can define a continuous angular coordinate $\varphi(\Theta,t)$, where the oscillator index is replaced by a continuous parameter $\Theta \in [0,2\pi]$. In the continuum limit, $N \to \infty$, the discrete oscillator index is replaced by the continuous parametrization variable Θ. Then, $\varphi(\Theta,t)$ describes the angular deviation of a respective chain segment from the angle Θ at time t, so that we can write $\varphi_i = \varphi(\Theta,t)|_{\Theta=i\,\Delta\Theta} + i\,\Delta\Theta$. Replacing the discrete Laplacian by a continuous second-order partial derivative, we arrive at

$$\ddot{\varphi}(\Theta,t) = -\gamma_\varphi(t)\,\dot{\varphi}(\Theta,t) + \kappa\,(\Delta\Theta)^2\,\frac{\partial^2\varphi(\Theta,t)}{\partial\Theta^2}. \tag{11}$$

We solve it through a separation of variables $\varphi(\Theta,t) = \Phi(\Theta)T(t)$, leading to

$$\frac{\ddot{T}}{T} + \gamma_\varphi\,\frac{\dot{T}}{T} = \kappa\,(\Delta\Theta)^2\,\frac{\Phi''}{\Phi} = \text{const.} \equiv -c^2.$$

The Θ-depending part has solutions of the form

$$\Phi(\Theta) = \Phi_a^0\,\sin\left(\frac{c}{\sqrt{\kappa}\,\Delta\Theta}\,\Theta\right) + \Phi_b^0\,\cos\left(\frac{c}{\sqrt{\kappa}\,\Delta\Theta}\,\Theta\right),$$

where Φ_a^0 and Φ_b^0 are constants of integration determined by the initial conditions. The periodic boundary conditions (closed chain) imply that $\Phi(\Theta) = \Phi(\Theta + 2\pi)$, which restricts the possible values of c to

$$c = m_\varphi\,\sqrt{\kappa}\,\Delta\Theta, \quad m_\varphi \in \mathbb{N}.$$

Along our line of reasoning, the value of m_φ determines the form of the longitudinal wave pattern. We recall that $\Phi(\Theta,t)$ quantifies the angular shift between the angle Θ and the angular coordinate of a chain segment assigned to Θ. The oscillation of Φ as a function of Θ suggests that the chain is alternatingly stretched and compressed in longitudinal direction compared to the positions of the oscillators in the minimum-energy configuration. The frequency of these variations increases with m_φ. Figure 4 shows the emergence of five stretched and five compressed chain sections, each one corresponding to a wave node of $\Phi(\Theta)$. Hence, this longitudinal wave has $m = 5$.

However, certain values of m_φ represent solutions of Eq. (11) that are incompatible with the full system Eq. (2). First, the Hamiltonian Eq. (1) is symmetric with respect to rotation around the origin. Therefore, the total angular momentum $\mathbf{L}$ is conserved. A longitudinal wave mode with $m_\varphi = 0$ violates this symmetry (see Appendix B), as

$$|\dot{\mathbf{L}}| = 0 \Leftrightarrow \int_0^{2\pi} \Phi(\Theta)\,d\Theta = 0 \Leftrightarrow m_\varphi \neq 0;$$

therefore, this value will be excluded. Similarly, due to the symmetry of the initial $k = 0$ phonon-like mode the total momentum $\mathbf{P} = \{P^x, P^y\}$ is conserved, up to corrections of the order of the random initial perturbations, as long as the chain remains in this setting. It does so from its preparation until the time of the onset of the emergence of either radial or longitudinal modes. We define this moment as $T_{\text{init}} = \min(\Gamma_\varphi^{-1}, \Gamma_r^{-1})$, with Γ_φ and Γ_r being the growth rates of the emerging longitudinal and radial wave modes; see Fig. 5. We do not expect longitudinal modes to break this principle. From Appendix B one gets

$$\dot{P}^{x/y}(t \ll T_{\text{init}}) \propto \int_0^{2\pi} \sin\Theta\,\sin(m_\varphi\,\Theta) = 0 \Leftrightarrow m_\varphi \neq 1,$$

and we can therefore exclude $m_\varphi = 1$.

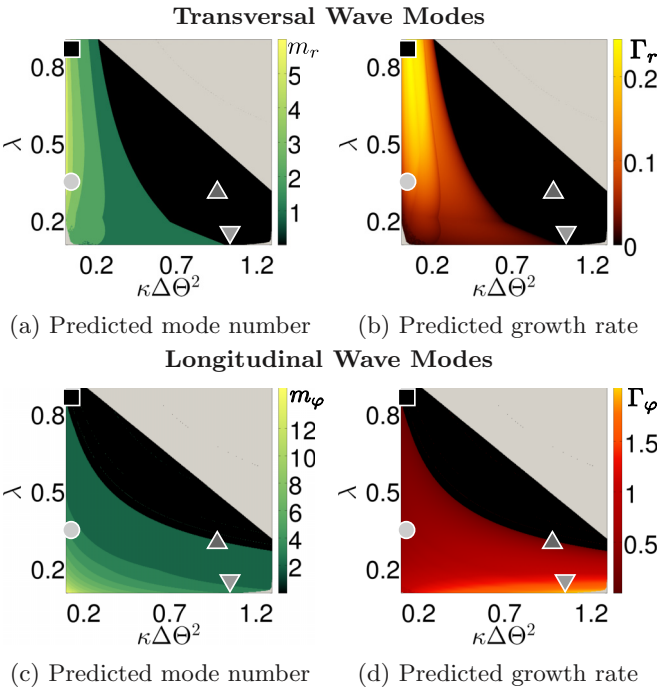

(a) Predicted mode number (b) Predicted growth rate

(c) Predicted mode number (d) Predicted growth rate

FIG. 5. (Color online) Analytical results from the study of emerging wave modes. Symbols (■▲▼●) indicate parameter choices according to Table I. $\epsilon_{\text{scale}} = 4$. No wave modes are expected in black areas; gray parameter areas are either excluded (Fig. 1) or their activation energy could not be determined (Fig. 11).

Finally, Eq. (11) was derived from a continuum limit. However, the original system has a finite number of oscillators. The boundary condition thus restricts the upper bound of m_φ to N as the number of oscillators. In summary, one has

$$m_\varphi = 2, 3, \ldots N.$$

In relation to Eq. (11), the time-dependent part can be interpreted as a parametric oscillator and its term containing the first time derivative is eliminated upon a transformation of variables

$$\tau(t) \equiv T(t) \exp \int_0^t \frac{\gamma_\varphi(\tilde{t})}{2} d\tilde{t} = T(t) \left[1 + \frac{A}{r^0} \sin(\omega_0 t)\right].$$

This leads to a Hill equation

$$\ddot{\tau} + c^2 \left[1 - \frac{\ddot{\tilde{r}}^0(t)}{c^2 \tilde{r}^0(t)}\right] \tau = 0, \tag{12}$$

where c is called the natural frequency and $-\ddot{\tilde{r}}^0(t) / [c^2 \tilde{r}^0(t)]$ is called pumping function.

The initial $k = 0$ phononlike chain setup produces negligible initial amplitudes of the longitudinal waves. Longitudinal waves will only emerge in the presence of a resonant growth in the solution of Eq. (12). We expect the emerging wave to possess the mode number that yields the largest growth rate. With the help of a Floquet stability analysis of the solutions of Eq. (12) we identify this value of m. Thus, we write Eq. (12) in the form

$$\frac{d}{dt}\begin{pmatrix}\dot{\tau}\\ \tau\end{pmatrix} = \begin{pmatrix}0 & -c^2\{1 - \ddot{\tilde{r}}^0(t)/[c^2 \tilde{r}^0(t)]\}\\ 1 & 0\end{pmatrix}\begin{pmatrix}\dot{\tau}\\ \tau\end{pmatrix}.$$

The pumping function is continuous and periodic (with period $\mathcal{T} = 2\pi/\omega_0$). Thus, Floquet theory applies and postulates the existence of a transition matrix $\underline{\underline{\rho}}$ that projects the current state vector $\{\tau(t), \dot{\tau}(t)\}$ onto the one after a period's time $\{\tau(t + \mathcal{T}), \dot{\tau}(t + \mathcal{T})\}$. Therefore, the eigenvalues, $\mu_{k=\{1,2\}}$, of $\underline{\underline{\rho}}$ determine the stability of the solution. It diverges if $|\mu_k| > 1$ for at least one k. Then, the growth rate of the longitudinal wave pattern is given by

$$\Gamma_\varphi = \frac{\ln\left(\max_k |\mu_k|\right)}{\mathcal{T}}.$$

To determine the transition matrix we (numerically) integrate Eq. (12) over one period for two linearly independent initial state vectors. Writing the initial state vectors as the columns of matrix $\underline{\underline{U_0}}$ and the state vectors after integration as columns of $\underline{\underline{U_1}}$, the transition matrix can be calculated from $\underline{\underline{U_1}} = \underline{\underline{\rho}}\,\underline{\underline{U_0}} \Rightarrow \underline{\underline{\rho}} = \underline{\underline{U_1}}\,\underline{\underline{U_0}}^{-1}$.

In order to determine the longitudinal mode number we first choose a certain energy. This defines the amplitude of the radial stimulus according to Eq. (9). Then, at each point in parameter space we scan through the range of possible values of m and determine the largest eigenvalue of the associated transition matrices. This value determines the growth rate of the longitudinal mode and the according m constitutes its wave number; see Figs. 5(c) and 5(d). Larger energies lead to an increase of mode numbers and their growth rates and shrink the parameter regions where no longitudinal wave modes are expected. The identification of these regions is a particularly important feature of our theory because the absence of longitudinal waves has a crucial impact on the distribution of energy among the different degrees of freedom (see Fig. 6) and thus on the escape behavior.

D. Interplay of transversal and longitudinal wave modes

The previous sections provide a theoretical framework describing the emergence of distinct wave patterns arising shortly after the initialization of the system. The associated wave mode numbers and growth rates are represented in Fig. 5.

For the long term behavior of the system the equations of motion Eq. (2) were integrated using a Runge-Kutta scheme of fourth order, choosing a time step small enough (typically of the order of 10^{-4}) to ensure that the energy deviation remains smaller than 10^{-12} throughout the entire simulation time.

Depending on the values of the parameters, we can identify three dynamical regimes characterized by the respective emerging wave modes, which govern how energy is transferred into different degrees of freedom. We monitor the temporal evolutions of the radial and longitudinal contributions to the kinetic energy,

$$\begin{aligned} E_{\text{kin}} &= \sum_{i=0}^{N-1} \frac{\mathbf{p}_i^2}{2} = \sum_{i=0}^{N-1} ((\mathbf{p}_i\,\mathbf{e}_r)\mathbf{e}_r + (\mathbf{p}_i\,\mathbf{e}_\varphi)\mathbf{e}_\varphi)^2 \\ &= \underbrace{\sum_{i=0}^{N-1} (\mathbf{p}_i\,\mathbf{e}_r)^2}_{E_{\text{kin}}^r} + \underbrace{\sum_{i=0}^{N-1} (\mathbf{p}_i\,\mathbf{e}_\varphi)^2}_{E_{\text{kin}}^\varphi}, \end{aligned} \tag{13}$$

as illustrated in Fig. 6.

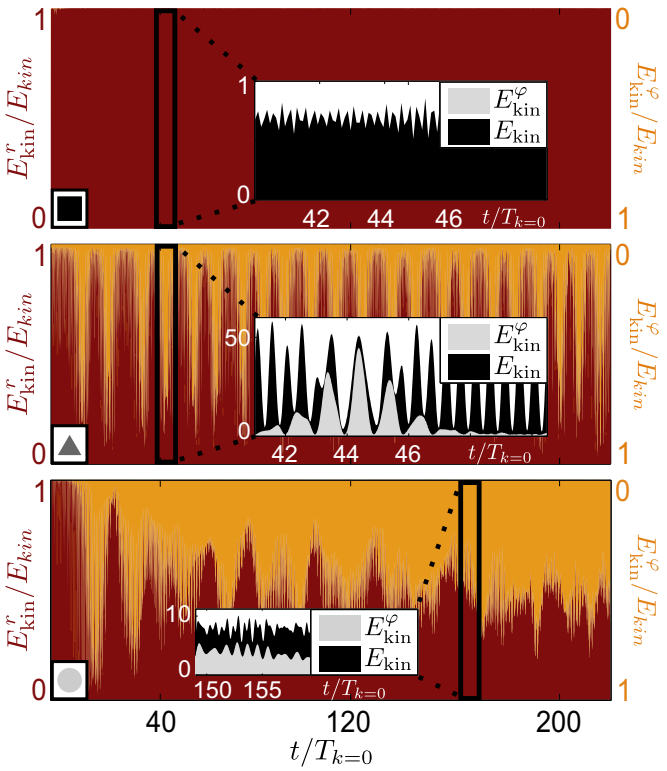

FIG. 6. (Color online) The background plots depict how the total kinetic energy divides among the longitudinal (yellow) and radial (red) contribution, $E^r_{\rm kin}$ and $E^\varphi_{\rm kin}$, as a function of time; see Eq. (13). The insets show the temporal evolution of absolute kinetic-energy values within the marked time frames. The three panels represent different parameter choices (indicated by the symbols ■▲● according to Table I), which represent the three different dynamical regimes as described in the text. Time is measured in units of $k = 0$ phonon periods $T_{k=0} = 2\pi/\omega_0$. For all choices of parameters, $\epsilon_{\rm scale} = 2$.

The system's behavior can be dominated by transversal wave modes. This is the case when longitudinal wave modes are absent [black areas in Figs. 5(c) and 5(d)] or when their mode number is high ($m_\varphi > 20$) as the associated angular displacement of individual oscillators remain small. In this case (even for large integration times in the order of the duration of many hundred phonon oscillations), energy transfer into longitudinal degrees of freedom is prevented (see "■" in Fig. 6: Virtually all kinetic energy is contained in the radial motion; due to the emergence of numerous, unsynchronized breathers the total kinetic energy remains approximately constant).

In the opposite case, where radial wave modes are absent or of high wave number ($m_r > 20$), the system's behavior will be dominated by longitudinal wave modes. As found in the previous section, these modes arise due to a resonant excitation from the initial phonon mode. With the growth of the longitudinal mode the system energy is transferred from the radial into the longitudinal degrees of freedom. However, once the phonon oscillations are attenuated the longitudinal modes can no longer be fed. Moreover, their amplitude will decrease, thereby leading the system back into the phononlike state. This again triggers the reemergence of the longitudinal wave. The system therefore resides in an oscillatory regime; see "▲" in Fig. 6. (In periodically repeating intervals nearly all of the kinetic energy is transferred into the longitudinal motion. Both the phonon and longitudinal mode cause a synchronous oscillation between kinetic and potential energy for each oscillator. This causes the oscillations of the total kinetic energy.)

In the simultaneous presence of radial and longitudinal wave modes, the system will develop a state of mode mixing leading to irregular long-term behavior. The resulting disordered state comprises a more homogeneous distribution of the system energy into all degrees of freedom; see "●" in Fig. 6. (After some initial longitudinal oscillations, the energy distribution approaches equipartition.)

Parameter choices that represent the three different regimes can be found in Table I.

TABLE I. Parameter choices.

	λ	$\kappa\,\Delta\Theta^2$	Description
■	0.85	1.25×10^{-4}	Dominant radial mode, $m_r \approx 18$
▲	0.4	1.00	Dominant longitudinal mode, $m_\varphi = 2$
▼	0.2	1.10	Dominant longitudinal mode, $m_\varphi = 3$
●	0.4	5.00×10^{-3}	Disordered regime

III. DETERMINISTIC ESCAPE

So far this analysis has focused on the description of emerging wave modes. However, we recall that the chain is initially placed in a metastable state. Ultimately, we are interested in the escape of the ring chain beyond the potential barrier into the unbounded regime.

A. Transition states and escape channels

In the context of the Hamiltonian dynamics with its fixed amount of total energy it is essential to know the minimal energy necessary for the system to leave the potential-energy basin for another region in configuration space, in other words the minimum energy needed for an escape event. This question leads to the search for first-order saddle points of the potential-energy surface. From the definition of the Hamiltonian, Eq. (1) follows the expression of the potential energy

$$U(\{\mathbf{q}_i\}) = \sum_{i=0}^{N-1}\left[\frac{\kappa}{2}(\mathbf{q}_i - \mathbf{q}_{i+1})^2 - \sqrt{\mathbf{q}_i^2} + \cos\left(\frac{\sqrt{\mathbf{q}_i^2}}{\lambda}\right)\right].$$

Thus, we solve $\nabla U(\{\mathbf{q}_i\}) = 0$, such that the Hessian matrix of U has only positive eigenvalues except for a single negative one. An algorithm originating from theoretical chemistry, the dimer method [15–18], proved effective to solve this numerically difficult task. It identifies a set of different saddle points of which most have no relevance to our study because they are either high-energy configurations, unattainable by our setting, or configurations that have already escaped from the metastable initial setting. There remain three transition state types, examples of which are shown in Fig. 7.

The existence of these transition states entails two different types of escape mechanisms. The escape related to transition

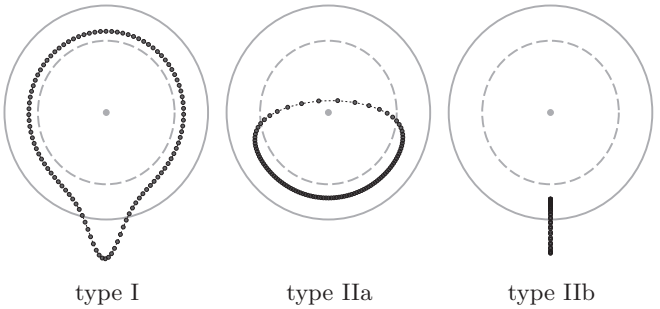

FIG. 7. Relevant transition state types.

state type I, as shown in Fig. 8, indicates a process in which a few oscillators surmount the potential barrier, are driven further down the outer slope of the potential barrier, and thereby pull out the entire chain from the metastable state. An escape of type II, depicted in Fig. 9, describes the process in which the chain first surmounts the central potential hump, passing the transition state of type IIa, and then overcomes the potential barrier in the way indicated by transition state type IIb.

The minimal energy necessary for an escape through channel I is the energy content of the transition state of type I. For an escape through channel II it is the larger one of the transition states energies of type IIa and IIb because the phase-space trajectory will have to pass through the vicinity of both transition states in order to leave the bounded regime.

Let us thus compare the energy values of different transition states (Fig. 10). This enables us to determine the minimal escape energy (Fig. 11), which will be referred to as the activation energy, E_{Act}. It is determined by the energy difference between the associated transition state and that of the minimum-energy configuration E_0. Thus, $E_{\mathrm{Act}} = \mathcal{H}(\{\mathbf{p}=0\},\{\mathbf{q}=\mathbf{q}^*\}) - E_0$, where $\{\mathbf{q}^*\}$ denotes the relevant transition state configuration. With this notion we define the energy scaling parameter:

$$\epsilon_{\mathrm{scale}} = \frac{E - E_0}{E_{\mathrm{Act}}}.$$

From now on, energies will only be expressed in terms of $\epsilon_{\mathrm{scale}}$, which is the ratio of the system's energy to the activation energy for a given set of parameters. This will not only allow us to evaluate the significance of the energy value with respect to the escape process but also to meaningfully compare energy values for different choices of parameter values.

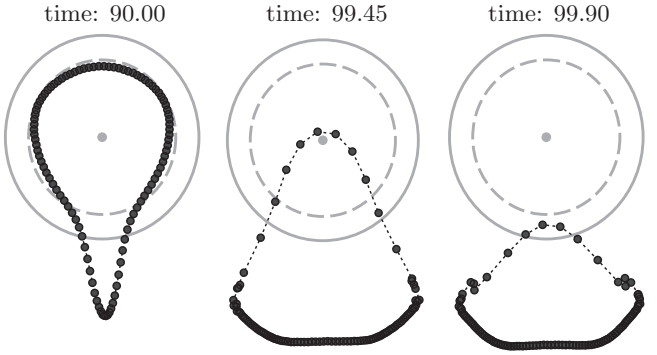

FIG. 8. Snapshots of an escape process of type I. Parameters: $\lambda = 0.8$, $\kappa\,\Delta\Theta^2 = 0.08$.

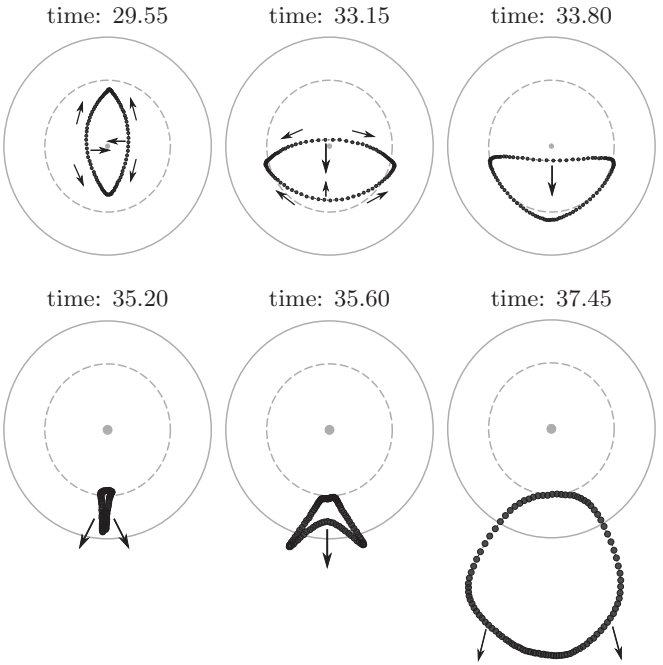

FIG. 9. Snapshots of an escape process of type II. Arrows indicate the chain movement. Parameters: "▲" according to Table I.

B. Escape times and characteristics

Figure 10 shows that for the largest portion of the relevant parameter space (red and blue areas) an escape through channel II is energetically more favorable. However, Sec. II revealed how different parameter values lead the system into different dynamical regimes which in turn influence the escape behavior. For a quantitative assessment of the deterministic escape we measure the escape times for the set of parameter choices given in Table I, as they represent a broad spectrum of the possible dynamical regimes.

To this end, we prepare ensembles of systems with equal parameter values and energies. The random perturbations of their initial conditions create different chain realizations that produce a statistical ensemble of escape times. The latter

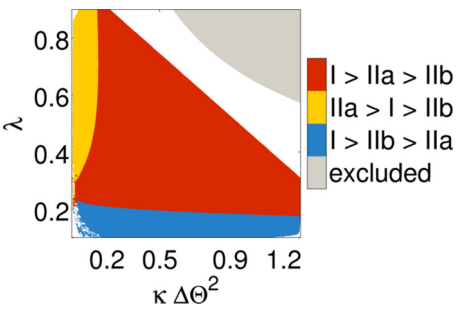

FIG. 10. (Color online) Comparison of the energies of different transition state types (white, no energy values determined; gray, excluded from parameter space).

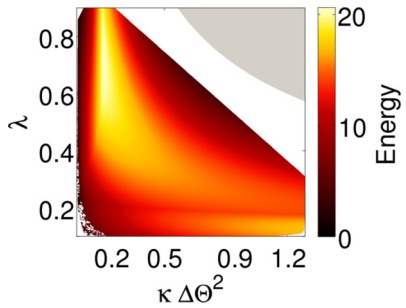

FIG. 11. (Color online) Activation energy corresponds to $\epsilon_{\text{scale}} = 1$ (white, no energy values determined; gray, excluded from parameter space).

are represented as cumulative escape time distributions in Fig. 12, which depicts the fraction of chains out of the total number of chain realizations, $N_T = 10^3$, that have escaped up until a certain time. The escape time is defined as the time it takes from the system's initialization until all oscillators have surpassed the potential barrier. To make escape times comparable between different sets of parameters we will measure them in units of $T_{k=0} = 2\pi/\omega_0$, that is, the duration of $k = 0$-mode phonon-like oscillations.

From Fig. 12 it is evident that different dynamical regimes relate to a different escape behavior. When the system's dynamics comprises a dominant transversal wave mode (■), it forms breathers that promote an escape of type I, as shown, e.g., in Fig. 3. Just as was observed in previous studies on deterministic escape of oscillator chain systems [7,19–22], breathers have the tendency to concentrate energy in small chain segments. The creation of these highly excited segments can produce critical oscillator elongations in radial direction

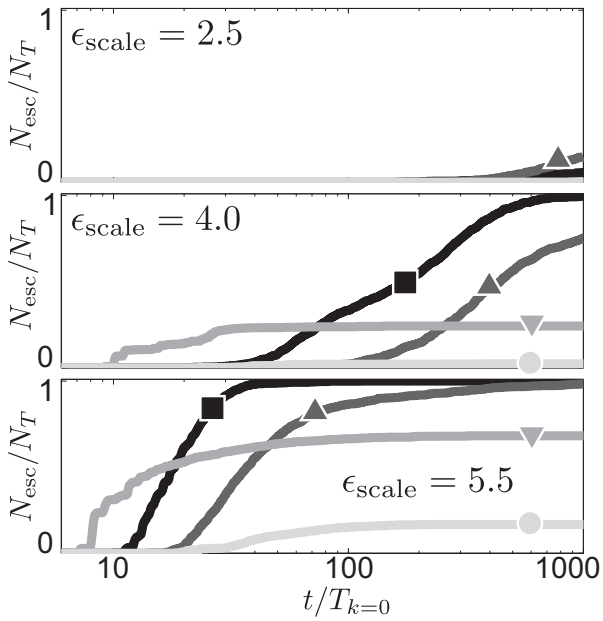

FIG. 12. Cumulative escape time distributions. Parameters (■: $m_r \approx 18$, ▲: $m_\varphi = 2$, ▼: $m_\varphi = 3$, ●: disordered regime) according to Table I.

beyond the potential barrier that trigger an efficient escape of type I.

In the presence of dominant longitudinal modes (▲, ▼) we observe an entirely different behavior with significant distinctions depending on the wave number m_φ. In general, an escape of type I is not expected because of the lack of energy concentration into critical radial elongations. However, we see an enhancement of an escape of type II if $m_\varphi = 2$ (▲). In such a case the chain is strongly stretched in between the two wave nodes. It tends to reduce the tension by decreasing the length of the stretched sections, which makes these more straight and they thereby surmount the central potential hump. The initial perturbations can break the symmetry of the longitudinal pattern, which can cause one of the two stretched segments to overcome the potential hump. Exactly this can be observed in the first three snapshots of Fig. 9. The first two snapshots show the two wave nodes (first vertically then horizontally aligned) and the third displays how the upper part of the stretched chain segment is carried over the potential hump. Generally, the subsequent trespass over the potential barrier is directly achieved due to the inert motion of the segment that was accelerated down the potential hump (this is because the energy of transition state type IIb is small whenever $m_\varphi = 2$). All in all, this mechanism triggers an enhanced escape of type II.

For dominant longitudinal modes of other wave numbers—already for $m_\varphi = 3$ (▼)—we no longer find this special geometry of the longitudinal wave and even for large energies an escape is inhibited. We do see initial escapes in this case, but those are only due to a high initial regular dynamics. When the $m_\varphi = 3$ mode is still mostly unperturbed it can cause some oscillator elongations in radial direction, which can initiate an escape of type I. Later on, when the longitudinal mode is more irregular, those escapes do not occur anymore so that the cumulative escape distribution (of ▼) completely saturates in the long run.

Finally, a system that evolves toward a highly irregular state (●), due to the mixing of longitudinal and transversal modes, also disperses the energy into all degrees of freedom (see bottom plot in Fig. 6). Thus, there is neither an energy concentration into transversal degrees of freedom causing an escape of type I nor the special geometry of the longitudinal mode bringing about an escape of type II. Again, we find initial escape events that take place before the modes have mixed, their type depending on which mode has a larger growth rate (here mostly escape type I). But once the chaotic state is attained, only on rare occasions can critical elongations drive the chain beyond the potential barrier. Hence, the escape is clearly inhibited compared to all other dynamical regimes.

IV. SUMMARY

We have studied the dynamics of a ring chain of interacting units and its escape over the brim of a Mexican-hat-like potential under microcanonical conditions. We have identified and analyzed the emergence of radial breather modes and longitudinal resonant wave modes emerging from a flat initial low-energy state. Depending on the parameter values we have classified the following three dynamical regimes: The system can either be dominated by one of the modes or will evolve

toward a highly irregular state. As demonstrated, this has a crucial impact on typical escape times.

Escape can be realized via two escape channels, which are related to different transition states. The escape through either of these channels is enhanced by breather modes. They efficiently accumulate energy into single radial degrees of freedom rendering single oscillators to pass over the potential's brim and subsequently pull the entire chain out of the metastable configuration. The second possibility is that the chain first overcomes the central potential hump and then surpasses the brim as a bundle. This escape path strongly relies on the presence of longitudinal resonant wave modes with wave number $m_\varphi = 2$. Notably, in both of these cases early escapes occur already for energy values in the order of a few times of the activation energy. Contrarily, the irregular dynamical regime practically prevents escape events, even for significantly larger energies.

In a more general context, this work shows that nonlinear cooperative effects among interacting units, which crucially impact the escape behavior, are not an inherent property of highly idealized systems but remain relevant for complex potential landscapes as well.

ACKNOWLEDGMENT

L. Schimansky-Geier thanks the Deutsche Forschungsgemeinschaft for support through Grant No. IRTG 1740.

APPENDIX A: STABILITY OF MINIMUM-ENERGY CONFIGURATION

The full-chain system as described by Eq. (2) has a fixed point, which is found for the coordinates (expressed in polar coordinates) $\varphi_i = i\,\Delta\Theta$, $r_i = r^0$, with r^0 defined in Eq. (5) (minimum-energy configuration), and momenta $\mathbf{p}_i = 0$. Let us examine its stability through a linear stability analysis. We thus investigate the system for small displacements $|\boldsymbol{\varepsilon}_{i,1}| \ll 1$ of the coordinates from the minimum-energy configuration and for small momenta $|\boldsymbol{\varepsilon}_{i,2}| \ll 1$. Neglecting all displacement terms of higher order, the linearized system can be written in block matrix form

$$\begin{pmatrix} \dot{\varepsilon^x}_{1,1} \\ \dot{\varepsilon^y}_{1,1} \\ \dot{\varepsilon^x}_{2,1} \\ \vdots \\ \dot{\varepsilon^y}_{N,1} \\ \dot{\varepsilon^x}_{1,2} \\ \vdots \\ \dot{\varepsilon^y}_{N,2} \end{pmatrix} = \underbrace{\begin{pmatrix} 0 & \cdots & 0 & & & \\ \vdots & \ddots & \vdots & & \mathbb{1}_{2N} & \\ 0 & \cdots & 0 & & & \\ & & & 0 & \cdots & 0 \\ & J_f & & \vdots & \ddots & \vdots \\ & & & 0 & \cdots & 0 \end{pmatrix}}_{\equiv \mathbb{M}} \begin{pmatrix} \varepsilon^x_{1,1} \\ \vdots \\ \varepsilon^y_{N,1} \\ \varepsilon^x_{1,2} \\ \vdots \\ \varepsilon^y_{N,2} \end{pmatrix}, \quad \text{(A1)}$$

where the Jacobi matrix J_f is defined as the matrix of all first partial derivatives of the right-hand side of Eq. (2) with respect to the coordinates, which takes the form

$$J_f = \begin{pmatrix} \aleph_{x,1} & \beth_1 & \kappa & 0 & 0 & & \cdots & & \kappa & 0 \\ \beth_1 & \aleph_{y,1} & 0 & \kappa & 0 & & \cdots & & 0 & \kappa \\ \kappa & 0 & \aleph_{x,2} & \beth_2 & \kappa & 0 & 0 & \cdots & & 0 \\ 0 & \kappa & \beth_2 & \aleph_{y,2} & 0 & \kappa & 0 & \cdots & & 0 \\ & & & & \vdots & & & & & \\ \kappa & 0 & 0 & & \cdots & & \kappa & 0 & \aleph_{x,N} & \beth_N \\ 0 & \kappa & 0 & & \cdots & & 0 & \kappa & \beth_N & \aleph_{x,N} \end{pmatrix},$$

with,

$$\aleph_{x,i} = -2\kappa + \frac{q_i^{y0}\, q_i^{y0}}{r^0\, r^0\, r^0}\left(1 + \frac{1}{\lambda}\sin\frac{r^0}{\lambda}\right) + \frac{q_i^{x0}\, q_i^{x0}}{\lambda^2\, r^0\, r^0}\cos\frac{r^0}{\lambda}$$

$$\aleph_{y,i} = -2\kappa + \frac{q_i^{x0}\, q_i^{x0}}{r^0\, r^0\, r^0}\left(1 + \frac{1}{\lambda}\sin\frac{r^0}{\lambda}\right) + \frac{q_i^{y0}\, q_i^{y0}}{\lambda^2\, r^0\, r^0}\cos\frac{r^0}{\lambda}$$

$$\beth_i = \frac{q_i^{x0}\, q_i^{y0}}{\lambda\, r^0 r^0}\left[-\frac{1}{r^0}\left(1 + \sin\frac{r^0}{\lambda}\right) + \frac{1}{\lambda}\cos\frac{r^0}{\lambda}\right].$$

The stability of Eq. (A1) can be inferred from the eigenvalues ν of $\mathbb{M}$. Its associated characteristic polynomial is defined as $\det(\mathbb{M} - \nu \cdot \mathbb{1}_{4N}) = 0$. The evaluation of the determinant can be simplified due to the block matrix structure of $\mathbb{M}$. As J_f and $(\nu \cdot \mathbb{1}_{2N})$ commute, we can reduce the problem to the eigenvalue problem for J_f (this can be seen from Leibniz formula for determinants) $\det(J_f - \nu^2 \cdot \mathbb{1}_{2N}) = 0$. J_f is symmetric and real. Therefore, its eigenvalues ν^2 are real as well. If any of them is positive the resulting pair of eigenvalues of $\mathbb{M}$, $\pm|\nu|$, includes a (real) positive eigenvalue and the fixed point is thus unstable. For the case $\nu^2 < 0$, the eigenvalues of $\mathbb{M}$ are purely imaginary and linear stability analysis fails to make predictions on the system's stability. However, recalling that the system is conservative a stability statement can yet be made. The Jacobi matrix J_f equals the (negative of the) Hessian matrix of the potential-energy function U (external potential plus coupling energy), and thus the eigenvalues ν^2 correspond to the negative curvature of the potential-energy surface along the eigenvectors. When all ν^2 are negative, the potential-energy surface has a minimum at the minimum-energy configuration. As the fixed point entails vanishing kinetic energy and energy is conserved, all phase-space trajectory in the vicinity of the fixed point are bound to the potential basin. Thus, in the case $\nu^2 < 0$ the fixed point is Lyapunov stable. The numerical solution of the eigenvalue problem of J_f for $N = 100$ yields Fig. 1. Decreasing the number of oscillators steadily enlargens the stable parameter region (e.g., $N = 10$: for $\lambda = 0.8$ the minimum-energy configuration is stable for coupling constants up to $\kappa\,\Delta\Theta^2 = 2.45$). However,

increasing the number, $N > 100$, does not significantly alter the regions of stability compared to $N = 100$.

APPENDIX B: TIME DERIVATIVE OF THE TOTAL (ANGULAR) MOMENTUM FOR THE LONGITUDINAL WAVE SOLUTION

The time derivative of the absolute value of the total angular momentum for N unit mass particles with polar coordinates r_i and φ_i, writes $|\dot{\mathbf{L}}| = \sum_{i=0}^{N-1} r_i(2\dot{r}_i\,\dot{\varphi}_i + r_i\,\ddot{\varphi}_i)$. To evaluate this expression for the longitudinal wave solutions we have to take the continuum limit and apply the expression for the radial components expressed in Eq. (10) and the solutions of Eq. (11) for the angular components. According to the earlier definitions this yields $r_i(t) \to \tilde{r}^0(t)$ and $\varphi_i(t) \to \varphi(\Theta,t) = \Phi(\Theta)\,T(t)$. Thus, the summation over all oscillators becomes an integral over Θ, such that

$$|\dot{\mathbf{L}}| = \tilde{r}^0\left(2\dot{\tilde{r}}^0\,\dot{T}\int_0^{2\pi}\Phi\,d\Theta + \tilde{r}^0\,\ddot{T}\int_0^{2\pi}\Phi\,d\Theta\right),$$

$$\Rightarrow |\dot{\mathbf{L}}| = 0 \Leftrightarrow \int_0^{2\pi}\Phi\,d\Theta = 0 \Leftrightarrow m_\varphi \neq 0.$$

For the time derivative of the total momentum we find

$$\dot{\mathbf{P}} = \sum_{i=0}^{N-1}\left(\ddot{r}_i - r_i\,\dot{\varphi}_i^2\right)\begin{pmatrix}\cos\varphi_i\\ \sin\varphi_i\end{pmatrix} + \sum_{i=0}^{N-1}\left(2\,\dot{r}_i\,\dot{\varphi}_i + r_i\,\ddot{\varphi}_i\right)\begin{pmatrix}-\sin\varphi_i\\ \cos\varphi_i\end{pmatrix}.$$

The conservation of the total momentum holds (up to corrections in the order of the initial random perturbations) as long as the chain resides in the $k = 0$ phonon-like state, in which $\varphi_i = i\,\Delta\Theta$. After its initial preparation, the chain remains in such a setting until the onset of either radial or longitudinal wave modes. Thus, we can define a point in time $T_{\text{init}} = \min(\Gamma_\varphi^{-1}, \Gamma_r^{-1})$ up until which the total momentum is conserved.

Taking the continuum limit and replacing the factors of the above equation by the according expressions in Eqs. (3) and (4), the initial total angular momentum writes

$$\begin{aligned}\dot{\mathbf{P}}(t \ll T_{\text{init}}) &= \int_0^{2\pi} d\Theta\left[1 + \frac{1}{\lambda}\sin\left(\frac{\tilde{r}^0(t)}{\lambda}\right)\right]\begin{pmatrix}\cos\Theta\\ \sin\Theta\end{pmatrix}\\ &\quad + \int_0^{2\pi} d\Theta\left[-\kappa\,(\Delta\Theta)^2\,\tilde{r}^0(t)\frac{\partial^2\varphi(\Theta,t)}{\partial\Theta^2}\right]\\ &\quad\times\begin{pmatrix}-\sin\Theta\\ \cos\Theta\end{pmatrix}\\ &\propto \int_0^{2\pi} d\Theta\left[\Phi_a^0\,\sin(m_\varphi\,\Theta) + \Phi_b^0\,\cos(m_\varphi\,\Theta)\right]\\ &\quad\times\begin{pmatrix}-\sin\Theta\\ \cos\Theta\end{pmatrix}\end{aligned}$$

$$\dot{\mathbf{P}}(t \ll T_{\text{init}}) = 0 \Leftrightarrow m_\varphi \neq 1.$$

[1] W. Sung and P. J. Park, Phys. Rev. Lett. **77**, 783 (1996).
[2] P. J. Park and W. Sung, Phys. Rev. E **57**, 730 (1998).
[3] I. E. Dikshtein, N. I. Polzikova, D. V. Kuznetsov, and L. Schimansky-Geier, J. Appl. Phys. **90**, 5425 (2001).
[4] K. L. Sebastian and A. K. R. Paul, Phys. Rev. E **62**, 927 (2000).
[5] S. K. Lee and W. Sung, Phys. Rev. E **63**, 021115 (2001).
[6] P. Kraikivski, R. Lipowsky, and J. Kierfeld, Europhys. Lett. **66**, 763 (2004).
[7] D. Hennig, L. Schimansky-Geier, and P. Hänggi, Europhys. Lett. **78**, 20002 (2007).
[8] T. Gross, D. Hennig, and L. Schimansky-Geier, in *First-Passage Phenomena and Their Applications* (World Scientific, Singapore, 2014), Chap. 22, pp. 554–570.
[9] J. Langer, Ann. Phys. **54**, 258 (1969).
[10] P. Hänggi, P. Talkner, and M. Borkovec, Rev. Mod. Phys. **62**, 251 (1990).
[11] S. D. Santos, V. Sánchez-Morcillo, N. Jiménez, A.-P. Abellard, and A. Bouakaz, AIP Conf. Proc. **1433**, 311 (2012).
[12] Y. S. Kivshar and M. Peyrard, Phys. Rev. A **46**, 3198 (1992).
[13] I. Daumont, T. Dauxois, and M. Peyrard, Nonlinearity **10**, 617 (1997).
[14] J. C. Eilbeck, P. S. Lomdahl, and A. C. Scott, Physica D **16**, 318 (1985).
[15] G. Henkelman and H. Jonsson, J. Chem. Phys. **111**, 7010 (1999).
[16] R. A. Olsen, G. J. Kroes, G. Henkelman, A. Arnaldsson, and H. Jonsson, J. Chem. Phys. **121**, 9776 (2004).
[17] A. Heyden, A. T. Bell, and F. J. Keil, J. Chem. Phys. **123**, 224101 (2005).
[18] A. Pedersen, S. Hafstein, and H. Jónsson, SIAM J. Sci. Comput. **33**, 633 (2011).
[19] D. Hennig, S. Fugmann, L. Schimansky-Geier, and P. Hänggi, Phys. Rev. E **76**, 041110 (2007).
[20] S. Fugmann, D. Hennig, L. Schimansky-Geier, and P. Hänggi, Phys. Rev. E **77**, 061135 (2008).
[21] S. Fugmann, D. Hennig, L. Schimansky-Geier, and I. Sokolov, Eur. Phys. J. Special Top. **191**, 187 (2011).
[22] S. Martens, D. Hennig, S. Fugmann, and L. Schimansky-Geier, Phys. Rev. E **78**, 041121 (2008).